8-26-2009

Transition to Mixing and Oscillations in a Stokesian Viscoelastic Flow

Becca Thomases
University of California, Davis, bthomases@smith.edu

Michael Shelley
Courant Institute of Mathematical Sciences

Recommended Citation

Transition to Mixing and Oscillations in a Stokesian Viscoelastic Flow

Becca Thomases[1] and Michael Shelley[2]

[1]*Department of Mathematics, University of California, Davis, California 95616, USA*
[2]*Courant Institute of Mathematical Sciences, New York University, New York, New York 10012, USA*
(Received 30 January 2009; published 26 August 2009)

In seeking to understand experiments on low-Reynolds-number mixing and flow transitions in viscoelastic fluids, we simulate the dynamics of the Oldroyd-B model, with a simple background force driving the flow. We find that at small Weissenberg number, flows are "slaved" to the extensional geometry imposed by forcing. For large Weissenberg number, such solutions become unstable and transit to a structurally dissimilar state dominated by a single large vortex. This new state can show persistent oscillatory behavior with the production and destruction of smaller-scale vortices that drive mixing.

PACS numbers: 47.50.−d

In low-Reynolds-number flow the nonlinearities provided by non-Newtonian stresses of a complex fluid can provide a richness of dynamics more commonly associated with high-Reynolds-number Newtonian flow. For example, experiments by Steinberg and collaborators have shown that dilute polymer suspensions being sheared in simple flow geometries can exhibit highly time-dependent dynamics and show efficient fluid mixing [1]. The same experiments using Newtonian fluids do not, and indeed cannot, show such nontrivial dynamics.

Extensional flows, as in a four-roll mill or in a cross-channel device, can be more effective in stretching and aligning polymers than a standard shear flow [2]. Therefore extensional flows may exhibit instabilities more readily than shearing flows. Experiments have shown that as polymer molecules pass near extensional stagnation points in a microchannel cross flow, they are strongly stretched and can exhibit nonlinear behavior such as bistability [2–4] (see also [5,6]). In observations of cross-channel flows, Arratia *et al.* [4] inferred molecular stretching through the appearance of two flow transitions with increasing flow rate. At the first, the flow remained steady but became asymmetrically deformed (see also [7,8]). At higher flow rates the velocity field fluctuated in time and produced fluid mixing. Numerical studies of this experiment have found instabilities for large Weissenberg number [9–11].

In this Letter we simulate the low-Reynolds-number dynamics of a viscoelastic fluid being driven by a simple background force. For a Newtonian fluid the forcing corresponds to a four-roll mill flow with a central stagnation point. Our viscoelastic simulations exhibit flow states qualitatively similar to those reported in [4], and can show fluid mixing as in [1]. In particular, we show that small perturbations from an isotropic initial stress field can induce a symmetry breaking transition that evolves to solutions that are qualitatively different in character from symmetric solutions, and from solutions at smaller Weissenberg number (which are essentially "slaved" to the background force). Beyond a first critical Weissenberg

number, the flow near the stagnation point becomes asymmetric and stretched, losing the symmetry of the background forcing. This new state appears steady. At yet higher Weissenberg number, the system transitions to a state dominated by a single large vortex and has persistent oscillations and a continual destruction and generation of smaller-scale vortices. These vortical oscillations can lead to mixing of the fluid across broad regions of the flow domain.

As our flow model, we adopt the Stokesian Oldroyd-B equations, given in dimensionless form by

$$-\nabla p + \Delta \mathbf{u} = -\beta \nabla \cdot \mathbf{S} + \mathbf{f} \quad \text{and} \quad \nabla \cdot \mathbf{u} = 0, \quad (1)$$

$$\mathbf{S}^{\nabla} = -(\mathrm{Wi})^{-1}(\mathbf{S} - \mathbf{I}) + \nu \Delta \mathbf{S}, \quad (2)$$

where $\mathbf{S}^{\nabla} \equiv \frac{\partial \mathbf{S}}{\partial t} + \mathbf{u} \cdot \nabla \mathbf{S} - (\nabla \mathbf{u} \cdot \mathbf{S} + \mathbf{S} \cdot \nabla \mathbf{u}^T)$. Here $\mathrm{Wi} = \tau_p/\tau_f$ is the Weissenberg number, with τ_p the polymer relaxation time and τ_f the time scale of the fluid flow. The external force, $\mathbf{f}$, drives the flow, and its dimensional scale F sets the flow time scale as $\tau_f = \mu/\rho LF$, where μ is the solvent viscosity, ρ the fluid density, and L the system length scale. With the particular choice here for $\mathbf{f}$, τ_f^{-1} is also the strain rate of extensional stagnation points in the induced Newtonian flow.

The parameter $\beta = G\tau_f/\mu$ measures the relative contribution of the polymer stress to momentum balance, where G is the isotropic stress induced by the polymer field in the absence of flow. The parameter ν controls polymer stress diffusion. Stress diffusion can arise when including the effect of center of mass diffusion of polymer coils [12]. Here it is added to control polymer stress gradient growth as Eqs. (1) and (2) otherwise lack a scale-dependent dissipation (see also [13–15] for other models incorporating stress diffusion). Aside from advectively driven gradient growth, there is stress growth related to the microscopic origins of the Oldroyd-B model [16,17]: the bulk fluid is assumed to be a Newtonian solvent with a dilute concentration of immersed polymer chains, them-

selves modeled as Hookean springs. This underlying as-
sumption can yield infinite viscosities at finite strain rates
for steady viscometric straining flows [17] (see also
[18,19]), and unbounded stress growth in time-dependent
flows [20] as a consequence of a coil-stretch transition.
Here we set $\nu = 10^{-3}$, which is sufficient to control **S** on
the time scales needed for these simulations. Last, the
quantity $\beta \cdot \mathrm{Wi}$ is the ratio of polymer to solvent viscosity
so that given a particular working fluid, its value is fixed
independent of experimental conditions. In the work of
Arratia *et al.* [4], $\beta \cdot \mathrm{Wi} \approx 0.5$, which is the value used
here.

Equations (1) and (2) are simulated in a 2D periodic box
$[-\pi, \pi]^2$. To obtain extensional stagnation points in the
flow, a steady spatially periodic background force is used,
$\mathbf{f} = (-2\sin x \cos y, 2\cos x \sin y)$, which for a Newtonian-
Stokes fluid yields a velocity field with a four-roll mill
geometry. The system is solved with a pseudospectral
method (see [20] for details). The high-wave number part
of the spatial Fourier spectrum is $\mathcal{O}(10^{-12})$ throughout the
simulations.

The initial data are a perturbation of the identity

$$\mathbf{S}_0 \equiv \mathbf{I} + \begin{pmatrix} \varepsilon_1 g(x)\cos(y) & -\varepsilon_2 \sin(x)\cos(2y) \\ -\varepsilon_2 \sin(x)\cos(2y) & \varepsilon_3 \cos(x)g(y) \end{pmatrix},$$
(3)

with $g(x) = 2\sin(x) - 3/2\sin(2x)$, and $\varepsilon_k = \mathcal{O}(10^{-2})$,
$k = 1, 2, 3$. The data are chosen so that the resulting
solution for the initial velocity field is a small perturbation
from the four-roll mill geometry, with initially unequal
vortical strengths. For example, for $\mathrm{Wi} = 10$, the vorticity
perturbation in quadrants I and III is roughly 3 times larger
than in quadrants II and IV. The perturbations in quadrants
I and IV are negative relative to the unperturbed state, and
in quadrants II and III are positive. Quadrant III receives a
slightly larger perturbation than quadrant I. The maximum
perturbation in the vorticity is $\mathcal{O}(10^{-3})$.

Figures 1 and 2 (and supplementary material [21]) show
the vorticity ω and polymer stress components both before
and after the onset of a symmetry breaking transition.
Figures 1(a), 2(a), and 2(b) are at $t = 100$, showing that
the initial near-symmetry of the dynamics is maintained
well into the evolution. At early times, $\mathrm{tr}\mathbf{S} = S_{11} + S_{22}$
(representing the mean-squared distension of polymer
coils) concentrates along the incoming and outgoing
streamlines of the extensional stagnation points in the
flow, and oppositely signed vortices arise along these
streamlines. These vortices are a consequence of the coil-
stretch transition which occurs for $\mathrm{Wi} \approx 1$ [20] and are not
seen for $\mathrm{Wi} < 1$. At $t \approx 200$, a symmetry breaking tran-
sition occurs, and the central stagnation point (CSP), ini-
tially at $(0, 0)$, migrates into quadrant I. The vortex in
quadrant I weakens relative to the vortex in quadrant III.

At even later times the flow becomes temporally and
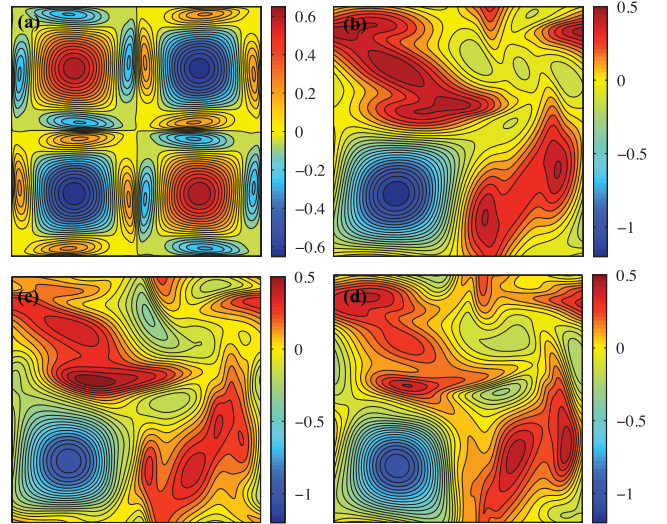spatially more complex. At $t \approx 1000$, a new and higher

FIG. 1 (color online).   Contour plot of vorticity field ω for
$\mathrm{Wi} = 10$, at $t = 100$ (a), 800 (b), 1400 (c), and 1700 (d). A
symmetry breaking transition occurs at $t \approx 200$, and the stag-
nation point at $(\pi/2, \pi/2)$ is destroyed at $t \approx 1000$.

frequency of flow oscillation emerges [Fig. 3(a) and [21]].
At that time the vestigial vortex center in quadrant I, still
seen in Fig. 1(b), is first destroyed, and the flow becomes
more complicated spatially thereafter, with patches of
positive and negative vorticity roiling about in quadrants
I, II, and IV [as in Figs. 1(c) and 1(d) and [21]].

The behavior at smaller Wi is quite different. For $\mathrm{Wi} \lesssim$
5 the velocity field remains slaved, like the Newtonian
case, to the background forcing, and perturbations in the
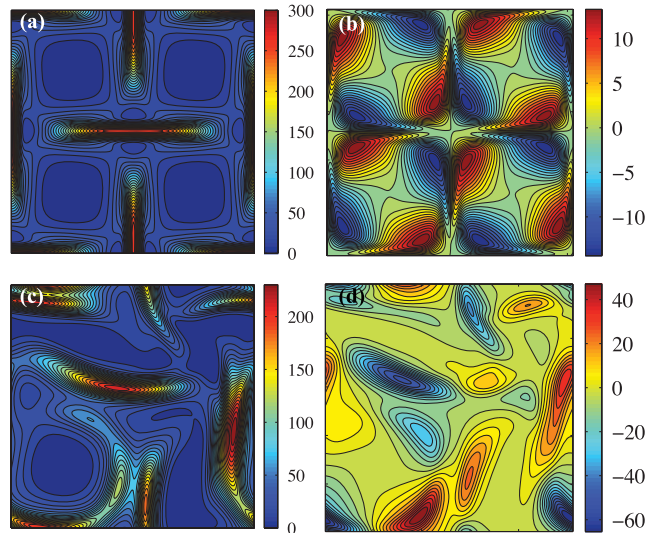initial data do not lead to symmetry breaking spatially. In

FIG. 2 (color online).   Contour plots of polymer stress compo-
nents for $\mathrm{Wi} = 10$. Panels (a) and (b) show $\mathrm{tr}\mathbf{S}$ and the shear
stress S_{12}, respectively, at $t = 100$, and panels (c) and (d) show
the same $t = 1400$. Note that the magnitude of $\mathrm{tr}\mathbf{S}$ is much larger
than that of S_{12}.

fact, if S_0 is chosen to be far from symmetric (say, by taking that from the Wi = 10 simulation at large times), and a simulation is performed with sufficiently small Weissenberg number (here Wi ≲ 5), the flow will relax to a steady symmetric state qualitatively similar to that in Figs. 1(a), 2(a), and 2(b).

Figure 3(a) shows the first component of velocity at a fixed point in the flow for Wi = 5, 6, and 10 with $0 \leq t \leq 5000$. For Wi = 5, the onset of the symmetry breaking transition occurs over a very long time, and the solution converges to a slightly asymmetric steady state, where the CSP sits in the first quadrant and the lower left vortex is slightly dominant. For Wi = 6 the onset of the symmetry breaking transition occurs more rapidly, after which there are decaying time-periodic oscillations in the velocity field, with relaxation to an asymmetric steady state. The asymmetry is more pronounced than for Wi = 5, and the CSP oscillates between the two upper quadrants before settling to a steady state in the upper half-plane. The streamlines of the steady state are seen in Fig. 4(a). The onset of the symmetry breaking transition occurs even more rapidly for Wi = 10, after which there are time-periodic oscillations in the velocity field and the CSP oscillates in the first quadrant. Again, at $t \approx 1000$ yet higher frequency, persistent oscillations appear [21]. (A simulation up to $t = 10\,000$ reveals no decrease in their amplitude.)

Figure 3(b) shows the temporal Fourier spectrum of $u(t)$ for Wi = 10. There are two fundamental frequencies, a and b, labeled in the plot. The first corresponds to the
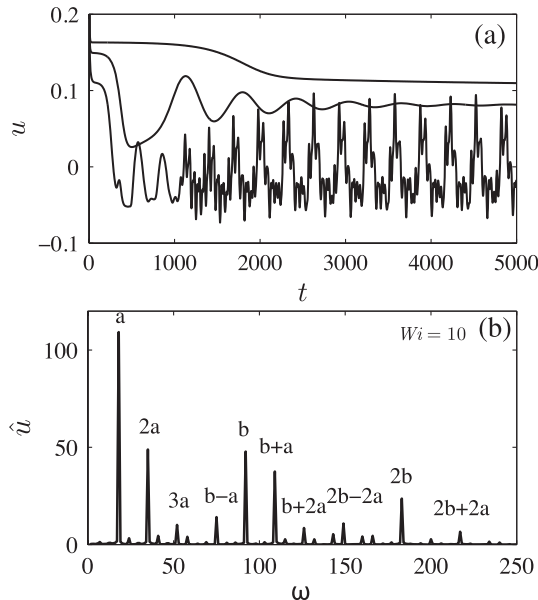
longer period $\tau \approx 317$, while the second arises as the vortex in the first quadrant is destroyed, and has period $\tau \approx 59$. The other activated frequencies are sums, differences, and harmonics of a and b. The spectrum at different points in the domain gives the same two dominant frequencies. The simulations indicate that $a \approx 0$ for Wi = 5 with a increasing with Wi. The second frequency b decreases with Wi and only arises for Wi ≳ 9. These high frequency oscillations lead to very complicated dynamics in the flow as can be seen in the late-time plots of the vorticity and stress [Figs. 1(c), 1(d), 2(c), and 2(d)].

Figure 4 shows how symmetry breaking and oscillations can produce fluid mixing in the system. We subdivide the 2π-periodic cell into quadrants, label fluid particles blue, green, red, and yellow (quadrants I through IV, respectively), and track them in the flow. For small Wi, say, Wi = 0.5, there is essentially no mixing among the four quadrants as the initial asymmetric perturbation relaxes away (not shown). Figure 4(a) shows the particle positions at $t = 2000$ for Wi = 6, as the system relaxes to steady state. While there has been considerable mixing, large regions of unmixed fluid remain corresponding to the perturbed, yet coherent vortices.

Very different are Figs. 4(b) and 4(c), which show the particle distributions for Wi = 10 at $t = 500$ and 2000,
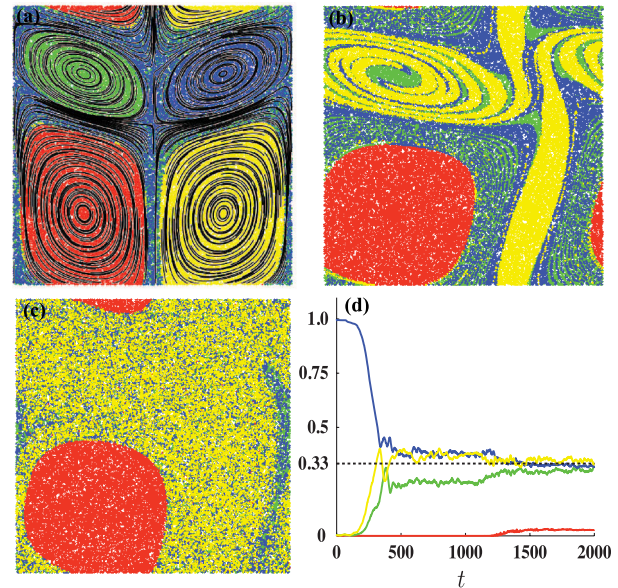

FIG. 4 (color online). Panels (a)–(c) show Lagrangian particle distributions from the numerical simulations (using 65 536 particles). Particles originating in quadrants I (upper right) through IV (lower right) are colored blue, green, red, and yellow, respectively. (a) Particle distribution for Wi = 6 at $t = 2000$ with streamlines of the steady state overlaid. (b) and (c) Particle distribution for Wi = 10 at $t = 500$ and 2000, respectively. (d) The percentage of particles of each color in quadrant I over time, $0 < t < 2000$. The dashed line at 1/3 shows the nearly equal representation of quadrants I, II, and IV over long times.

FIG. 3. (a) The first component of the velocity field at a fixed point versus time $[u(t) = u_1(\pi/4, \pi/4, t)]$ for Wi = 5 (upper curve), 6 (middle curve), and 10 (lower curve). (b) The temporal spectrum of $u(t)$ for Wi = 10 with the transform taken over late times.

respectively. Figure 4(b) shows layers of particles from quadrants I, II, and IV mixing and interleaving, while 4(c) shows the emergence of a well-mixed fluid outside of the large stable vortex of quadrant III. Figure 4(d) shows the percentage of each color in quadrant I as a function of time. This quadrant is singled out because of the specific structure of the asymmetric state, and gives time scales of the observed processes. Under transit to the asymmetric state, the fluid begins to mix outside the stable vortex, as seen in 4(b). However, with the onset of higher frequency vortical oscillations for $t > 1000$, there is more significant mixing of particles from three of the four quadrants, with red particles from the remaining vortex also being stripped away and mixed. The coherent vortical structure which remains is reminiscent of the persistent elliptic regions found in experiments of Newtonian flows at an intermediate Reynolds number driven by an array of magnets and associated Lorenz forces [22]. Those patterns are periodic recurrences in response to a periodic driving force, but the remaining vortex here arises from a steady force and is not associated with any recurrences.

In conclusion, we find that in this simple theoretical setting, viscoelastic fluids can exhibit two transitions. The first is to a steady asymmetric state, and the second to persistent oscillations at multiple frequencies. This second, higher Weissenberg number state produces fluid mixing over broad regions of the flow. These results seem similar to observations of Arratia *et al.* [4] and of Groisman and Steinberg [1]. Unlike those experiments, we do not find broadband activity in temporal spectra, but instead several active discrete modes. Another interesting observation concerns the early part of the oscillatory phase of the flow. Though the initial data slightly perturb the locations of all of the stagnation points, we find that the flow relaxes into a complex dynamics with no obvious symmetries and yet has stagnation points refixed at the vortex centers of the Newtonian flow (even though the flow there may not be elliptical). At higher Wi the appearance of faster oscillations destroys this pinning, and more rapid mixing begins. One important question is how the evolution of the system depends upon the initial data. In trials with initial stress taken as random perturbations from the identity, the qualitative features of the transitions are robust, although the ultimate location of the persistent vortex displays a complicated dependence on the initial data. It is noteworthy that in one such trial the vortex does not relax to a single quadrant, but instead switches dynamically and persistently from quadrant to quadrant [21]. If instead the forcing is perturbed and is strongest in a quadrant, then that quadrant's vortex will become dominant over long times. This suggests possible protocols for global mixing of the fluid, for example, by using relaxation interleaved with biased forcing that exploits the multistability of the asymmetric state. We have also found similar dynamics in simulations of the FENE-P model [23] which limits the

growth of polymer stress through introduction of a length constraint to polymer stretching. More detailed studies are ongoing. Future work includes investigations into the origins of the instability via bifurcation and stability analysis. Finally, other modes of instability are available in three dimensions, and we anticipate yet richer behavior there [24].

[1] A. Groisman and V. Steinberg, Nature (London) **405**, 53 (2000); Nature (London) **410**, 905 (2001); New J. Phys. **6**, 29 (2004).

[2] D. E. Smith, H. P. Babcock, and S. Chu, Science **283**, 1724 (1999).

[3] C. M. Schroeder *et al.*, Science **301**, 1515 (2003).

[4] P. E. Arratia *et al.*, Phys. Rev. Lett. **96**, 144502 (2006).

[5] P. G. de Gennes, J. Chem. Phys. **60**, 5030 (1974).

[6] E. J. Hinch, in *Polymeres et Lubrification Colloques International du C.N.R.S.* (Editions du CNRS, Paris, 1974), Vol. 233, p. 241.

[7] A. Groisman, M. Enzelberger, and S. Quake, Science **300**, 955 (2003).

[8] L. E. Rodd *et al.*, J. Non-Newtonian Fluid Mech. **129**, 1 (2005).

[9] R. J. Poole and M. A. Alves, and P. J. Oliveira, Phys. Rev. Lett. **99**, 164503 (2007).

[10] L. Xi and M. Graham, J. Fluid Mech. (to be published).

[11] S. Berti *et al.*, Phys. Rev. E **77**, 055306(R) (2008).

[12] A. W. El-Kareh and L. G. Leal, J. Non-Newtonian Fluid Mech. **33**, 257 (1989).

[13] C. Y. Lu, P. D. Olmsted, and R. C. Ball, Phys. Rev. Lett. **84**, 642 (2000).

[14] E. J. Hinch, J. Non-Newtonian Fluid Mech. **54**, 209 (1994).

[15] J. M. Rallison, J. Non-Newtonian Fluid Mech. **68**, 61 (1997).

[16] M. Doi and S. Edwards, *The Theory of Polymer Dynamics* (Oxford University Press, New York, 1986).

[17] R. Larson, *The Structure and Rheology of Complex Fluids* (Oxford University Press, New York, 1998).

[18] E. J. Hinch, Phys. Fluids **20**, S22 (1977).

[19] M. Renardy, J. Non-Newtonian Fluid Mech. **138**, 204 (2006).

[20] B. Thomases and M. Shelley, Phys. Fluids **19**, 103 103 (2007).

[21] See EPAPS Document No. E-PRLTAO-103-065936 for four supplementary movies, showing the dynamics of the flow and stress field for Wi $= 10$. For more information on EPAPS, see http://www.aip.org/pubservs/ epaps.html.

[22] G. A. Voth, G. Haller, and J. P. Gollub, Phys. Rev. Lett. **88**, 254501 (2002).

[23] R. Bird, P. Dotson, and N. Johnson, J. Non-Newtonian Fluid Mech. **7**, 213 (1980).

[24] R. G. Larson, E. Shaqfeh, and S. J. Muller, J. Fluid Mech. **218**, 573 (1990).